

Computer Vision, Graphics, and Pattern Recognition Group
Department of Mathematics and Computer Science
University of Mannheim
D-68131 Mannheim, Germany

Variational Optical Flow Estimation for Particle Image Velocimetry

P. Ruhnau¹, T. Kohlberger¹, C. Schnörr¹, H. Nobach²

¹Department of Mathematics and Computer Science
Computer Vision, Graphics, and Pattern Recognition Group
University of Mannheim, 68131 Mannheim, Germany
{ruhnau,tiko,schnoerr}@uni-mannheim.de
www.cvgpr.uni-mannheim.de

²Chair of Fluid Mechanics and Aerodynamics
Darmstadt University of Technology, 64287 Darmstadt, Germany
holger.nobach@nambis.de
www.sla.maschinenbau.tu-darmstadt.de

The publications of the CVGPR Group are listed under
<http://www.cvgpr.uni-mannheim.de>

Variational Optical Flow Estimation for Particle Image Velocimetry

P. Ruhnau¹, T. Kohlberger¹, C. Schnörr¹, H. Nobach²

¹Department of Mathematics and Computer Science
Computer Vision, Graphics, and Pattern Recognition Group
University of Mannheim, 68131 Mannheim, Germany
{ruhnau,tiko,schnoerr}@uni-mannheim.de
www.cvgpr.uni-mannheim.de

²Chair of Fluid Mechanics and Aerodynamics
Darmstadt University of Technology, 64287 Darmstadt, Germany
holger.nobach@nambis.de
www.sla.maschinenbau.tu-darmstadt.de

Abstract

We introduce a novel class of algorithms for evaluating PIV image pairs. The mathematical basis is a continuous variational formulation for globally estimating the optical flow vector fields over the whole image. This class of approaches has been known in the field of image processing and computer vision for more than two decades but apparently has not been applied to PIV image pairs so far.

We pay particular attention to a multiscale representation of the image data so as to cope with the quite specific signal structure of particle image pairs. The experimental evaluation shows that a prototypical variational approach competes in noisy real-world scenarios with three alternative approaches especially designed for PIV-sequence evaluation. We outline the potential of the variational method for further developments.

Keywords: Particle image velocimetry, particle tracking, optical flow, variational methods

1 Introduction

Particle Image Velocimetry (PIV) is an important and active research field concerned with the quantitative investigation of fluids by imaging techniques [17]. The prevailing technique underlying most computational approaches to estimating the motion of fluids from corresponding image pairs is based on the correlation of local interrogation windows in subsequent frames. However, despite the success of this technique and numerous investigations into improvements (which are summarized in [18]), it suffers from some fundamental limitations:

- The partitioning of the image by interrogation areas must not be too fine if you want to detect correlation peaks reliably. This unavoidably limits the spatial resolution of the estimated motion vector field. The advanced hierarchical schemes described in [18] offer the possibility of ending with very small interrogation areas. However, even in these high-performance techniques, post-processing is necessary to detect erroneous motion vectors.

- The size of the interrogation areas determines a spatial scale at which the variation of motion vector fields is (tacitly) assumed to be negligible. This assumption is erroneous and proves inaccurate in many relevant situations. Many authors have concentrated on iterative window deformation methods of 1st or 2nd order that deal with this problem [18].
- Motion estimation is carried out regardless of spatial context. As a consequence, prior knowledge about spatial flow structures cannot be exploited during estimation, and missing motion estimates in image regions where a correlation analysis yields no reliable estimates, have to be heuristically inferred in a post-processing step.

The objective of this paper is to introduce a novel class of motion estimation approaches to the PIV-community. The prototypical approach of this class is due to Horn and Schunck [9], and many corresponding approaches have been analyzed in the fields of image processing and computer vision. For a review and extensions we refer to [23]. In this paper, we focus on the prototypical approach [9] along the analysis presented in [19]. The variational framework and corresponding features will be presented in section 2. Next, we carefully examine features of a coarse-to-fine implementation, thus taking into account the specific gray value-functions induced by particles in PIV image pairs (section 3). Numerical experiments for benchmark image pairs and a comparison with two alternative approaches especially designed for PIV-sequence evaluation will be presented in section 4. We conclude in section 5 by indicating extensions of the prototypical approach within the variational framework.

2 Variational Approach

2.1 Basic Assumptions and Constraints

Let $f(x, y, t)$ denote the gray value recorded at location $(x, y)^\top$ and time t in the image plane. A basic assumption underlying most approaches to motion estimation is that f is conserved, that is the change of $f(x, y, \cdot)$ at location $(x, y)^\top$ is due to a movement of $f(x, y, t)$ to the location $(x + u\Delta t, y + v\Delta t)^\top$ during a time intervall Δt :

$$f(x + u\Delta t, y + v\Delta t, t + \Delta t) = f(x, y, t) . \quad (1)$$

A common approach to estimating the *optical flow vector* $(u, v)^\top$ at some fixed location $(\bar{x}, \bar{y})^\top$ on the image grid $(x, y)^\top = (k\Delta x, l\Delta y)^\top$, $k, l \in \mathbb{Z}$, is to assume u and v to be constant within a local spatial area $N(\bar{x}, \bar{y})$ around $(\bar{x}, \bar{y})^\top$ and to minimize¹

$$\sum_{k, l \in N(\bar{x}, \bar{y})} [f(k + u\Delta t, l + v\Delta t, t + \Delta t) - f(k, l, t)]^2 \quad (2)$$

as a function of u and v . Assuming additionally that $\sum_{k, l \in N(\bar{x}, \bar{y})} f(k, l, t)^2$ does not vary with $(\bar{x}, \bar{y})^\top$, the minimizing values of u, v maximize the correlation function

$$\sum_{k, l \in N(\bar{x}, \bar{y})} f(k + u\Delta t, l + v\Delta t, t + \Delta t) f(k, l, t) .$$

¹Without loss of generality we take $\Delta x = \Delta y = 1$

The first major difference to variational approaches is that the latter explicitly take into account smooth changes of the flow $(u, v)^\top$ at time t as a function of x and y : $u = u(x, y), v = v(x, y)$. A continuously formulated expression analogous to (2) then reads:

$$\int_{\Omega} [f(x + u(x, y)\Delta t, y + v(x, y)\Delta t, t + \Delta t) - f(x, y, t)]^2 dx dy \quad (3)$$

Note that since we do no longer assume u and v to be piecewise constant according to a subdivision of the visible section Ω of the image plane into interrogation areas, we integrate over the entire image domain Ω , observing the Neumann border conditions. From the viewpoint of variational analysis and algorithm design, formulation (3) is less favourable because the dependency on u and v is highly non-convex. A common way around this difficulty is (i) to further simplify the objective function so as to obtain a mathematically tractable problem, and (ii) to apply the resulting variational approach to a multi-scale representation of the image data f (see section 3) so that the following approximation becomes valid:

$$\begin{aligned} & f(x+u\Delta t, y + v\Delta t, t + \Delta t) \\ & \approx f(x, y, t) + \partial_x f(x, y, t)u\Delta t + \partial_y f(x, y, t)v\Delta t + \partial_t f(x, y, t)\Delta t \\ & = f(x, y, t) + \nabla f(x, y, t) \cdot \begin{pmatrix} u \\ v \end{pmatrix} \Delta t + \partial_t f(x, y, t)\Delta t \end{aligned} \quad (4)$$

where the spatial and temporal derivatives of f can be estimated locally using FIR filters (see section 4.2.).

Inserting this approximation into (1) (and dropping the argument (x, y, t) for convenience) yields:

$$\nabla f \cdot \begin{pmatrix} u \\ v \end{pmatrix} + \partial_t f = 0. \quad (5)$$

According to computer vision literature, this is the so-called *Brightness Change Constraint Equation (BCCE)* which merely reflects with a differential formulation our basic assumption (1) made in the beginning:

$$\frac{d}{dt}f(x, y, t) = 0 = \nabla f \cdot \begin{pmatrix} \dot{x} \\ \dot{y} \end{pmatrix} + \partial_t f$$

Using (4) and (5), the objective function (3) becomes:

$$\int_{\Omega} [\nabla f \cdot \begin{pmatrix} u \\ v \end{pmatrix} + \partial_t f]^2 dx dy \quad (6)$$

Note that this objective function now depends *quadratically* on the two functions $u(x, y)$ and $v(x, y)$, which is much more convenient from the mathematical point-of-view! So far, the transition to a continuous setting has led us to the formulation (6) which has to be minimized with respect to arbitrary functions u and v . Clearly, this problem is not well-posed as yet because *any* vector field with components $\nabla f \cdot (u, v)^\top = -\partial_t f, \forall x, y$, is a minimizer. However, rather than to consider vector fields which are piecewise constant within interrogation areas, we merely rule

out too irregular vector fields by additionally minimizing the magnitudes of the spatial gradients of u and v :

$$J(u, v) = \int_{\Omega} \left\{ \left[\nabla f \cdot \begin{pmatrix} u \\ v \end{pmatrix} + \partial_t f \right]^2 + \lambda (|\nabla u|^2 + |\nabla v|^2) \right\} dx dy, \quad 0 < \lambda \in \mathbb{R}. \quad (7)$$

Parameter λ is either a user-parameter or can be determined as Lagrange multiplier related to the either of the constraints

$$\begin{aligned} \int_{\Omega} \left[\nabla f \cdot \begin{pmatrix} u \\ v \end{pmatrix} + \partial_t f \right]^2 dx dy &= \alpha, \\ \int_{\Omega} (|\nabla u|^2 + |\nabla v|^2) dx dy &= \beta, \end{aligned}$$

provided either of the numbers α or β is known. The discussion of this and other possible extensions is however beyond the scope of this paper (cf. section 5), and we regard λ as a user-parameter. In view of the limitations mentioned in section 1, we point out the following features of the variational approach (7):

- The approach is formulated in terms of *functions* u and v and hence, by definition, provides motion estimates $(u(x, y), v(x, y))^{\top}$ at *any point* $(x, y)^{\top} \in \Omega \subset \mathbb{R}^2$.
- Spatial variation of u, v is merely constrained by a *global* penalty term (i.e. the second term in (7)). Accordingly, the motion field $(u, v)^{\top}$ may exhibit spatial variations of different strengths depending on the evidence provided by the spatio-temporal image sequence data f .
- The approach is intrinsically non-local and allows to incorporate spatial context in a mathematically convenient way by means of functionals depending on u, v and corresponding derivatives.

2.2 Optimization Problem and Discretization

Under mild conditions with respect to the image sequence data f it can be shown [19] that the functional (7) is strictly convex. As a consequence, the *Finite Element Method (FEM)* can fully be exploited, as will be sketched next. For details we refer to [6, 21]. The unique globally minimizing vector field $(u(x, y), v(x, y))^{\top}$ is determined by the variational equation

$$a((u, v)^{\top}, (\tilde{u}, \tilde{v})^{\top}) = b((\tilde{u}, \tilde{v})^{\top}), \quad \forall \tilde{u}, \tilde{v}, \quad (8)$$

where

$$a((u, v)^{\top}, (\tilde{u}, \tilde{v})^{\top}) = \int_{\Omega} \left\{ \begin{pmatrix} u \\ v \end{pmatrix} \cdot \nabla f \nabla f \cdot \begin{pmatrix} \tilde{u} \\ \tilde{v} \end{pmatrix} + \lambda (\nabla u \cdot \nabla \tilde{u} + \nabla v \cdot \nabla \tilde{v}) \right\} dx dy, \quad (9)$$

$$b((\tilde{u}, \tilde{v})^{\top}) = - \int_{\Omega} \partial_t f \nabla f \cdot \begin{pmatrix} \tilde{u} \\ \tilde{v} \end{pmatrix} dx dy. \quad (10)$$

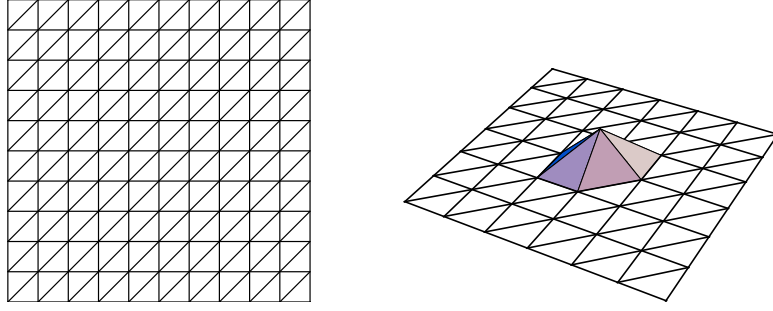


Figure 1: **Left:** Uniform triangulation of the image domain Ω . **Right:** Basis function $\phi_i(x, y)$ attached to pixel position i .

The simplest discretization is obtained by choosing a regular triangulation of the image domain Ω and attaching to each pixel position a piecewise linear basis function $\phi(x, y)$ for each function $u, v, \tilde{u}, \tilde{v}$, as illustrated in Figure 1. Indexing each pixel position (k, l) by $1, 2, \dots, N$ we thus have

$$u(x, y) = \sum_{i=1}^N u_i \phi_i(x, y) ,$$

and similarly for v, \tilde{u}, \tilde{v} . Hence, each of the functions $u, v, \tilde{u}, \tilde{v}$ is represented by N real variables. To simplify notation, we use the same symbols to denote these vectors: $u, v, \tilde{u}, \tilde{v} \in \mathbb{R}^N$. Inserting into (8) leads to:

$$\begin{pmatrix} u \\ v \end{pmatrix} \cdot A \begin{pmatrix} \tilde{u} \\ \tilde{v} \end{pmatrix} = b \cdot \begin{pmatrix} \tilde{u} \\ \tilde{v} \end{pmatrix} , \quad \forall \tilde{u}, \tilde{v} ,$$

hence:

$$A \begin{pmatrix} u \\ v \end{pmatrix} = b \tag{11}$$

The $2N \times 2N$ -Matrix A factorizes into

$$A = \begin{pmatrix} A_{11} & A_{12} \\ A_{12}^\top & A_{22} \end{pmatrix}$$

where by virtue of (9):

$$\begin{aligned} (A_{11})_{k,l} &= a((\phi_k, 0)^\top, (\phi_l, 0)^\top) \\ (A_{12})_{k,l} &= a((\phi_k, 0)^\top, (0, \phi_l)^\top) \\ (A_{22})_{k,l} &= a((0, \phi_k)^\top, (0, \phi_l)^\top) . \end{aligned}$$

Analogously, the $2N$ -vector b factorizes into $b = (b_1^\top, b_2^\top)^\top$ where by virtue of (10):

$$\begin{aligned} (b_1)_k &= b((\phi_k, 0)^\top) \\ (b_2)_k &= b((0, \phi_k)^\top) . \end{aligned}$$

The linear system (11) is sparse and positive definite. Thus u, v can be conveniently computed by some corresponding iterative solver [8].

3 Coarse-to-Fine Motion Estimation

The accuracy of motion estimation critically depends on the magnitude of image motion. In fact, depending on the spatial image frequency, very large motions even may cause aliasing along the time frequency axis. For illustration, Figure 2 shows a 1D-signal moving to the right at constant speed u :

$$g(x, t) = \sin(\omega_x(x - ut)). \quad (12)$$

Due to the Nyquist-condition $|\omega_t| < \pi$ (with $\omega_t := \omega_x u$), only motions up to $|u| < \pi/\omega_x$ are correctly represented by samples of the signal.² Faster motions lead to aliasing. In other words, for a fixed global velocity, spatial frequencies moving more than half of their period per frame cause temporal aliasing. In practice, this upper bound has to be lowered because derivatives of the signal can only be robustly estimated in connection with low-pass filtering.

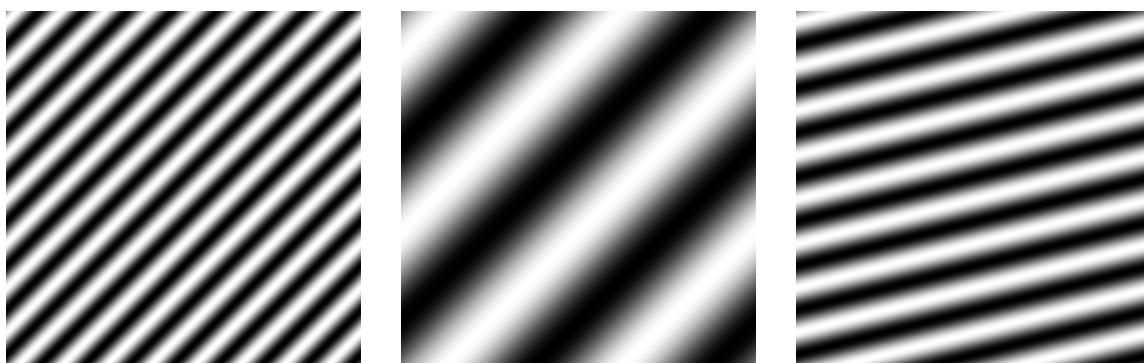


Figure 2: Moving signal $g(x, t) = \sin(\omega_x(x - ut))$ as gray value image with different parameters ω_x (spatial frequency) and u (velocity). **Left:** $\omega_x = \pi/4$, $u = 1$, **Middle:** $\omega_x = \pi/16$, $u = 1$, **Right:** $\omega_x = \pi/16$, $u = 4$. Temporal frequency is affected by both spatial frequency ω_w and velocity u .

As a remedy, we first compute a coarse motion field by using only low spatial frequency components and “undo” the motion, thus roughly stabilizing the position of the image over time. Then the higher frequency subbands are used to estimate optical flow on the warped sequence. Combining this “optical flow correction” with the previously computed optical flow yields a refined overall optical flow estimate. This process may be repeated at finer and finer spatial scales until the original image resolution is reached [12, 22]. A standard technique for generating multi-scale representations in this context is to construct an image pyramid (Figure 3) by recursively applying lowpass filtering and subsampling operations. Note that the images at different scales are represented by different sampling rates. Thus, the same derivative filters may be used at each scale and we do not have to design multiple derivative filters, one for each different scale. Let us define the pyramid representation of a generic image f of size $n_x \times n_y$. Let $f^0 = f$ be the “zeroth” level image. This image is essentially the highest resolution image (the raw image). The image width and height at that level are defined as $n_x^0 = n_x$ and $n_y^0 = n_y$. The pyramid representation is then built in a recursive fashion: Compute f^1 from f^0 , then compute f^2 from f^1 , and so on Let $k = 0, 1, 2, \dots, L - 1$ be a generic pyramidal level, and let f^k be the image at level k . n_x^k and n_y^k denote the width and the height of f^k . First the lowpass filter $[1/4 \ 1/2 \ 1/4] \times [1/4 \ 1/2 \ 1/4]^T$ is used for image anti-aliasing before image subsampling. Then a bilinear interpolation performs the adaption to the new coarser

²Without loss of generality we assume sampling rates $\Delta x = \Delta t = 1$.

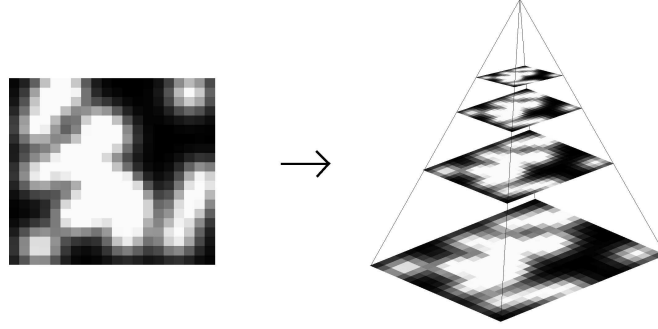


Figure 3: Image Pyramid: Each level in the pyramid is a subsampled version of the level below convolved with a Gaussian filter.

grid, as every new vertex is located exactly in the middle of four finer vertices (if the respective image size is even-numbered, cmp. Figure 4). This procedure results in a convolution mask of $[1/8 \ 3/8 \ 3/8 \ 1/8] \times [1/8 \ 3/8 \ 3/8 \ 1/8]^T$. In the first step the optical flow between the top level

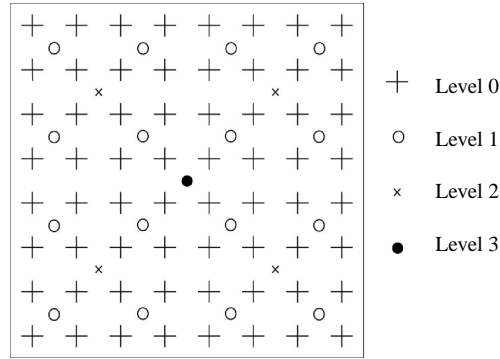


Figure 4: Image Pyramid: Location of the vertices in the respective levels.

images f_1^{L-1} and f_2^{L-1} (lowest frequency images) is computed, using the variational approach of section 2. The computed coarse-level flow field must then be projected onto the next finer pyramid level. This flow field estimate is used to warp the second image towards the first image:

$$\mathcal{W}\{f_2^{L-1}, d^{L-1}\}(x, y, t + \Delta t) = f_2^{L-1}(x - u\Delta t, y - v\Delta t, t + \Delta t), \quad d^{L-1} = \begin{pmatrix} u \\ v \end{pmatrix} \quad (13)$$

At pyramid level $L - 2$, we compute a new and finer flow field between the images f_1^{L-2} and $\mathcal{W}\{f_2^{L-2}, d^{L-1}\}$. While the expression to be minimized is analogous to (7), the first-order Taylor series expansion is performed around $(x + d^{L-1}(x), t + 1)$. This results in the cost functional:

$$J(u, v) = \int_{\Omega} \left\{ \left[\nabla f \cdot \begin{pmatrix} u \\ v \end{pmatrix} + \partial_t f \right]^2 + \lambda (|\nabla(u + d_u^{L-1})|^2 + |\nabla(v + d_v^{L-1})|^2) \right\} dx dy, \quad 0 < \lambda \in \mathbb{R}. \quad (14)$$

The unique flow field minimizing (14) is the correction-field Δd^{L-2} of the coarser flow field d^{L-1} . In order to obtain the overall flow field d^{L-2} at level $L - 2$ we have to add the coarse motion d^{L-1} and the correction field Δd^{L-2} :

$$d^{L-2}(x, y) = d^{L-1}(x, y) + \Delta d^{L-2}(x, y) \quad (15)$$

This correction process is repeated for each level of the pyramid until the finest pyramid level d^0 has been reached. In the experimental evaluation section below, we will refer to this approach as Horn & Schunck Multi-Resolution (**H&S R**). So far, we have introduced a *dyadic* pyramid structure which is equivalent to using lowpass filters with bandwidths $\frac{\Omega}{2^{L-1}}, \frac{\Omega}{2^{L-2}}, \dots, \frac{\Omega}{2^1}, \frac{\Omega}{2^0}$ combined with subsampling. Now we introduce additional filters that slice the bandwidth into even smaller pieces, e.g. $\Omega/4, 3/8\Omega, \Omega/2, 3/4\Omega, \Omega$. In order to implement these extra steps which do not fit into the dyadic pyramid structure, we apply at each pyramid level pre-filters when estimating derivatives. Figure 5 shows the effect on a typical particle image: the lower the cut-off frequency of the pre-filter, the more the particles seem to melt down and form a smooth gray value structure. A coarse motion estimate can reliably be computed using this structure. Then, we update and refine the motion field (in the same way as described in detail for the multi-resolution case) using the less low-pass filtered image derivatives. Figure 6 shows

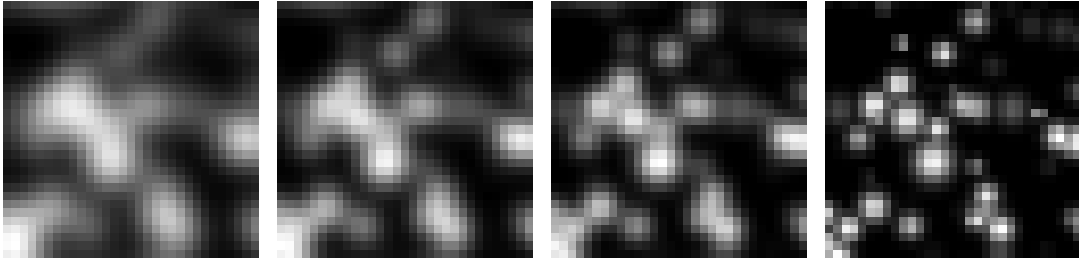


Figure 5: A sample particle image in different scale levels.

the frequency spectra of the Gaussian filters we apply, for the case of five scale-space levels. In practice, we use nine scale-space levels and thus nine different filters with cut-off frequencies of $\frac{\pi}{2}, \frac{9}{16}\pi, \frac{5}{8}\pi, \frac{11}{16}\pi, \frac{3}{4}\pi, \frac{13}{16}\pi, \frac{7}{8}\pi, \frac{15}{16}\pi, \pi$. An inverse Fourier Transform yields the filter coefficients. Low pass filtering with cut-off frequencies below $\pi/2$ is not necessary, since this is what the anti-aliasing filter of the preceding lower resolution level has already done.

Below, we will refer to this combined approach as Horn&Schunck Multi-Resolution + Multi-Scale (**H&S R+S**).

4 Experimental Evaluation

In this section, we report comparisons of the variational approach with three other approaches for various data sets. Before discussing the results in section 4.4 below, we first describe the data sets used for the comparison (section 4.1), the alternative approaches (besides the variational approach) and corresponding parameter setting (section 4.2) and quantitative error measures (section 4.3).

4.1 Data

The experimental evaluation was carried out on the basis of the following data sets:

- **Quénot image pair:** The first set of artificial benchmark image pairs was introduced in [16] and is available on the internet. The analyzed velocity field (av. velocity = 7.58 pixels/frame) is taken from a numerical solution, obtained for two-dimensional flow around a pair of cylinders (Figure 7).

We examined ten different test cases belonging to the following four classes:

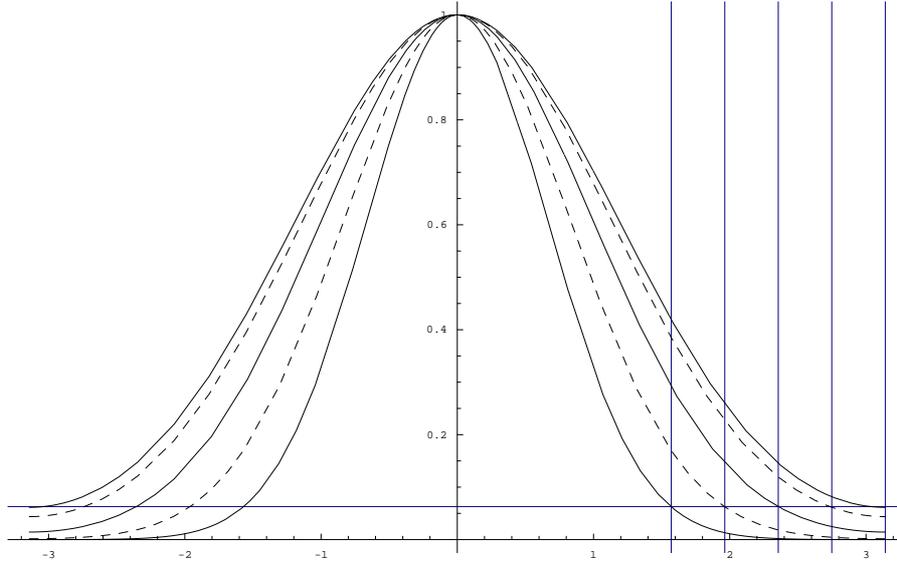


Figure 6: Gaussian Filters with cut-off frequencies of $\pi/2$, $5/8\pi$, $3/4\pi$, $7/8\pi$, π .

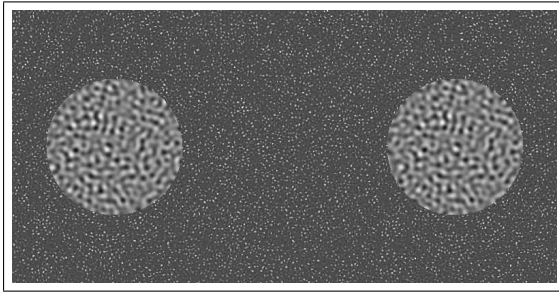


Figure 7: Quénot image pair: synthetic particle image

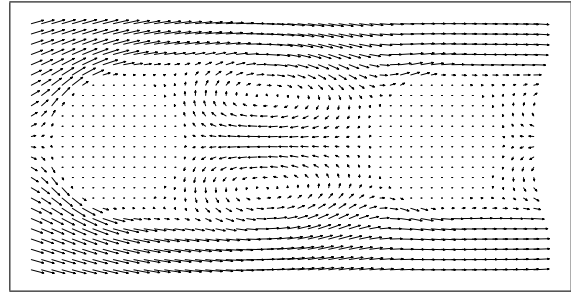


Figure 8: Exact velocity field (av. 7.58 px/frame)

- **Perfect:** “Perfect” case means that the second image was computer-generated from the first image and the target flow field.
 - **Noise N%:** Additionally to the “perfect” case, noise was superimposed for all images.
 - **Add/Rm N%:** The specified percentage of particles was randomly removed and the same amount of particles was randomly added.
 - **Mixed N%:** In this case all images were corrupted by both types of errors (Noise N% and Add/Rm N%) simultaneously.
- **VSJ:** In 1999, the Visualization Society of Japan (VSJ) published standard PIV images on their website [13]. There are eight different computer-generated standard image pairs. They differ from each other in image features as well as in flow field attributes.

Table 1 lists the parameters of these standard images: The number of particles that are present in the images, the particle diameter and the standard deviation of the particle diameter, the average image velocity and the out-of-plane velocity. The average image velocity defines the particle displacement in the image between two successive images. The target velocity field (Figure 10) is scaled in order to achieve a certain average image velocity. This is equivalent to adapting the temporal sampling rate.

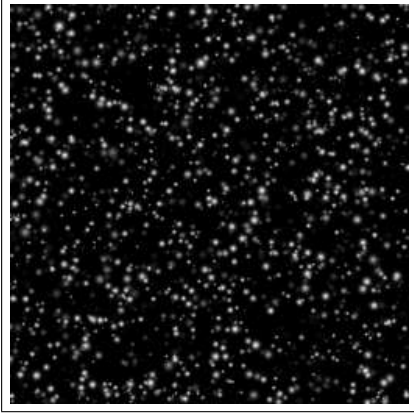


Figure 9: Sample VSJ standard image

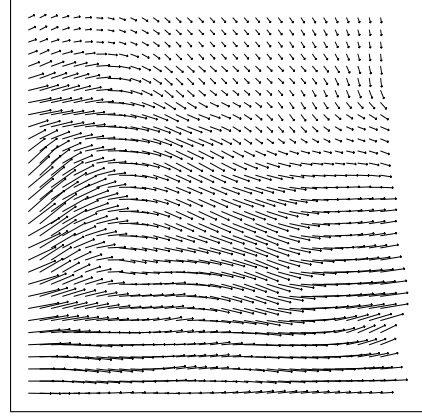


Figure 10: Exact velocity field

The out-of-plane velocity expresses the three-dimensional effects of the flow field: The intensity of the particles that move slightly out of the plane fades, and if the particle completely leaves the plane the gray value of the particle disappears.

Table 1 shows that some parameters were varied while others were kept constant: For image pairs 01, 04 and 05, for example, the number of particles is 1,000, 4,000 and 10,000, while all other parameters are fixed. The image pairs 01, 02 and 03 differ only with respect to the magnitude of the flow field: the average velocities are 2.5, 7.4 and 22 pixels/frame but the flow field structure is the same in all three cases.

Image	Av. Displacement	Max. Displacement	Av. Out of Plain Vel.	Number of Particles	Av. Particle Diameter d	Std. Deviation of d
01	7.4 px	15.0 px	0.017	4000	5.0 px	1.4 px
02	22.0 px	45.00 px	0.058	4000	5.0 px	1.4 px
03	2.5 px	5.1 px	0.006	4000	5.0 px	1.4 px
04	7.4 px	15.0 px	0.017	10000	5.0 px	1.4 px
05	7.4 px	15.0 px	0.017	1000	5.0 px	1.4 px
06	7.4 px	15.0 px	0.017	4000	5.0 px	0.0 px
07	7.4 px	15.0 px	0.017	4000	10.0 px	4.0 px
08	7.4 px	15.0 px	0.170	4000	5.0 px	1.4 px

Table 1: Pre-generated VSJ standard images. Variations from the default settings are marked in bold font.

- **Real-world images:** We also included two real-world image pairs into our data set. Figure 11 shows a corresponding image from the first test case of a time-resolved PIV measurement of periodical vortices in the transitional cylinder wake [3, 25]. The mean displacement is about 9 pixels/frame and the maximum displacement about 16 pixels/frame. Figure 18 shows the second real-world test case: freezing in a convection box filled with water [16]. The mean displacement in this case is about 4 pixels/frame and the maximum about 15 pixels/frame.

4.2 Approaches and Parameter Settings

The data sets described above were evaluated using the following approaches and parameter settings:

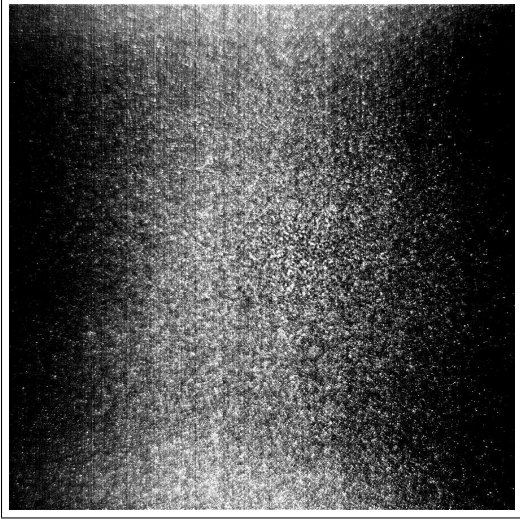


Figure 11: Real-world image

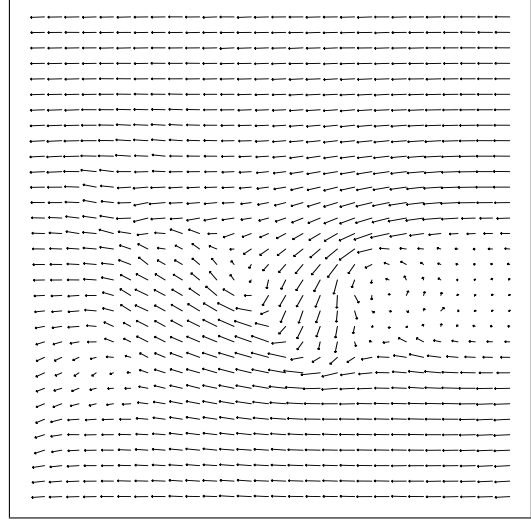


Figure 12: Estimated flow field (variational approach)

- **Variational approach:** The spatial (∇f) and temporal ($\partial_t f$) derivatives were estimated using derivative of Gaussian filters of size five at every point in the image domain. At the image borders (where the filter mask hangs over the image) the image is mirrored about its edge pixel (for smoothing operations) or reflected and inverted (for derivative operations).

In a first series of experiments (**H&S R**) five resolution levels were used, in a second series of experiments (**H&S R+S**), a setup of five resolution levels and nine scale space levels on every resolution level was chosen. For the Quénot image pair computations, the smoothness parameter λ was set to $7 * 10^{-4}$ in the H&S R case and to $7 * 10^{-3}$ in the H&S R+S case. For the VSJ and the real-world image pairs, only H&S R+S computations were performed. The smoothness parameter λ was also set to $7 * 10^{-3}$ in these rows of experiments. This value was determined experimentally. However, we will show in section 4.4 that, up to a certain point, changes of λ do not deteriorate results distinctly and that one can even improve the results by adapting λ manually. The gray values were scaled in each case to the interval $[0, 1]$.

- **DIPV approach:** For comparison we took the error measures of the classical 2D FFT based digital particle image velocimetry (DPIV) method from [16] in the synthetic test cases. Two different interrogation window sizes were applied: 32×32 pixel (**DPIV 32**) and 48×48 pixel (**DPIV 48**). We analyzed the “cylinder wake” real-world image pair using a hierarchical DPIV approach, with an interrogation window size beginning with 512×512 pixels and ending up with 64×64 pixels, with window-shifting and peak-height validation (but without substitution or interpolation, as we want to compare the actually computed values).
- **ODP2 approach [15]:** We also considered the results of a dynamic programming based optical flow technique. This approach transforms the two-dimensional correspondence problem to a sequence of one-dimensional search problems. It has been successfully applied to particle image velocimetry in [16]. The error measures were taken from [14].
- **KLT approach [5]:** Finally, we considered the results of a feature-tracking approach

to motion estimation. The Kanade-Lucas-Tomasi Tracker tracks local areas of sufficient intensity variation; outliers are erased and a dense motion field is interpolated.

4.3 Error Measures

As quantitative error measures we computed the angular error (between correct and computed motion vectors) as defined in [1] along with its standard deviation as well as the mean velocity error (L_1 norm of the difference between the correct and the computed velocities in pixels/frame).

For the Quénot image pair, the error measure was computed for the whole image except for the inner circular regions corresponding to the cylinders. Since the VSJ standard image pairs have different average velocities, the relative L_1 norm error (absolute error divided by average in-plane velocity) was computed in the corresponding series of experiments for the sake of comparability.

4.4 Numerical Results and Discussion

4.4.1 Quénot Image Pair

Table 2 summarizes the error measures and their standard deviation (\pm)³. Furthermore, typical execution times of the respective algorithms are indicated.

		DPIV32	DPIV48	ODP2	KLT	H&S R	H&S R+S
Perfect	angle	5.95 ± 13.9	9.35 ± 18.3	1.23 ± 2.24		2.32 ± 3.69	1.42 ± 2.16
	disp	0.55 ± 0.94	0.87 ± 1.46	0.13 ± 0.10	0.30 ± 0.80	0.39 ± 0.66	0.19 ± 0.18
Noise 5%	angle	6.49 ± 14.6	9.69 ± 19.0	1.83 ± 3.84		2.88 ± 4.21	1.53 ± 2.29
	disp	0.61 ± 1.18	0.86 ± 1.49	0.21 ± 0.46	0.30 ± 0.80	0.45 ± 0.67	0.21 ± 0.26
Noise 10%	angle	8.75 ± 17.9	10.8 ± 20.0	4.01 ± 10.8		4.02 ± 5.51	1.77 ± 2.65
	disp	0.77 ± 1.57	0.91 ± 1.59	0.53 ± 1.44	0.31 ± 0.60	0.60 ± 0.75	0.24 ± 0.41
Noise 20%	angle	35.0 ± 35.5	31.0 ± 30.4	6.70 ± 11.8		7.13 ± 8.95	2.52 ± 3.62
	disp	3.11 ± 4.14	2.06 ± 2.88	0.88 ± 1.58	0.42 ± 0.60	1.10 ± 1.13	0.33 ± 0.49
Add/rm 5%	angle	6.04 ± 13.8	9.35 ± 18.3	1.27 ± 2.35		2.48 ± 3.91	1.43 ± 2.17
	disp	0.55 ± 0.90	0.86 ± 1.45	0.14 ± 0.11		0.46 ± 0.82	0.19 ± 0.20
Add/rm 10%	angle	5.94 ± 13.5	9.52 ± 18.5	2.61 ± 9.94		2.62 ± 4.10	1.48 ± 2.31
	disp	0.55 ± 0.93	0.87 ± 1.47	0.34 ± 1.28		0.54 ± 0.97	0.21 ± 0.33
Add/rm 20%	angle	6.11 ± 14.2	9.77 ± 19.2	1.42 ± 2.54		3.41 ± 4.94	1.54 ± 2.50
	disp	0.56 ± 0.99	0.88 ± 1.52	0.16 ± 0.12		0.99 ± 1.67	0.23 ± 0.43
Mixed 5%	angle	6.40 ± 14.4	9.59 ± 19.0	1.77 ± 2.87		3.04 ± 4.38	1.54 ± 2.34
	disp	0.60 ± 1.12	0.86 ± 1.51	0.20 ± 0.13		0.52 ± 0.80	0.21 ± 0.30
Mixed 10%	angle	10.2 ± 19.6	11.3 ± 20.8	4.30 ± 11.7		4.39 ± 5.89	1.81 ± 2.74
	disp	0.91 ± 1.89	0.93 ± 1.66	0.57 ± 1.71		0.78 ± 1.07	0.26 ± 0.46
Mixed 20%	angle	40.8 ± 34.5	38.3 ± 29.7	6.15 ± 9.01		9.33 ± 9.93	2.96 ± 4.23
	disp	3.73 ± 4.39	2.49 ± 3.19	0.74 ± 0.52		2.03 ± 2.13	0.39 ± 0.53
Time		10 min	10 min	20 min	15 sec	16 sec / 2 sec	2 min / 15 sec

Table 2: Angular error and absolute displacement error. Best performance for every setting is marked in bold.

³Error measures for the three algorithms not implemented by the authors were taken from [16], the execution times from [5].

Note that DPIV and KLT yield sparse vector fields, whereas both ODP2 and the variational approach compute dense vector fields. All of the tested algorithms are rather insensitive to particle appearance/disappearance. However, they all are (in varying degrees) sensitive to superimposed noise. In the case of DPIV, extending the interrogation window size increases the robustness to noise, while decreasing the accuracy at the same time. However, irrespective of the window size, the performance of DPIV is much worse than the performance of the other approaches.

Comparing H&S R and H&S R+S, we realize that H&S R+S provides much better results in all the test cases. This had to be expected because temporal aliasing as well as linearization errors due to eqn. (4) are suppressed by additional scale space computations.

Figure 13 shows the results for the “Mixed 20%” test case. One can see that the highest estimation errors are reached at the borders of the two cylinders. The smoothness term penalizes the discontinuities at these locations and smoothes over the discontinuities. The error at regions close to the left cylinder is the highest because of the high velocity of the fluid. In section 5 we will point out possible solutions to this problem such as the insertion of border conditions and higher order regularization.

The two lower images of figure 13 compare the exact vorticity field and the estimated vorticity field using our approach. With exception of the addressed problem (flow discontinuity at the left cylinder), the estimated vorticity field resembles the exact vorticity field very well.

ODP2 provides the best result for the “perfect” test case. However, it is much less robust to noise than H&S: While the error measures of the variational coarse-to-fine approach are slightly higher in the perfect case (cf. table 2), this changes with the presence of noise. The error for the ODP2 approach then rises much faster, so that, for noise rates of 5 % and above, the H&S R+S approach provides better results. This gap rises even more for higher amounts of noise. Since noise is always present in real-world image pairs, we expect the variational Horn & Schunck algorithm to perform better than both the DPIV and the ODP2 approaches.

The error measures of KLT are consistently better than those of H&S R, but slightly worse than the results of ODP2 and H&S R+S. However, it seems to be less noise sensitive than ODP2, and has the advantage of much faster execution times than this computationally expensive dynamic programming technique.

When we use a preconditioned conjugate gradient method to solve the H&S system matrices, the execution time of our algorithm is about 16 sec for H&S R and 2 min for H&S R+S (when choosing a residual error of 10^{-4} as a stopping criterion). Using a multi-grid approach [2, 7] to solve the linear systems, the computation time of H&S R is approx. 2 sec, while the H&S R+S computation takes about 15 sec on an up-to-date computer. Information about the different multi-grid cycles and stopping criterions can be taken from [4]. Thus our approach is as fast as the feature tracker and faster than ODP2. Even real time operation can be achieved through parallelization using domain decomposition [11]. Note, however, that, while we use a 3 GHz Intel processor, the DPIV and ODP results were obtained using much older and slower machines. Quénot mentions in [16] a 250 MHz SGI processor and a 200 MHz Intel processor.

4.4.2 VSJ Standard Image Pairs

Figure 14 compares the average L_1 errors of ODP2 and H&S R+S for all eight VSJ standard image pairs. The average relative L_1 error of the H&S R+S computation for image pairs 01 and 04-07 is constantly between 1.89 (image pair 04 has a high particle density) and 3.51 (image pair 05 has a low particle density). As a consequence, the number of particles seems to be the

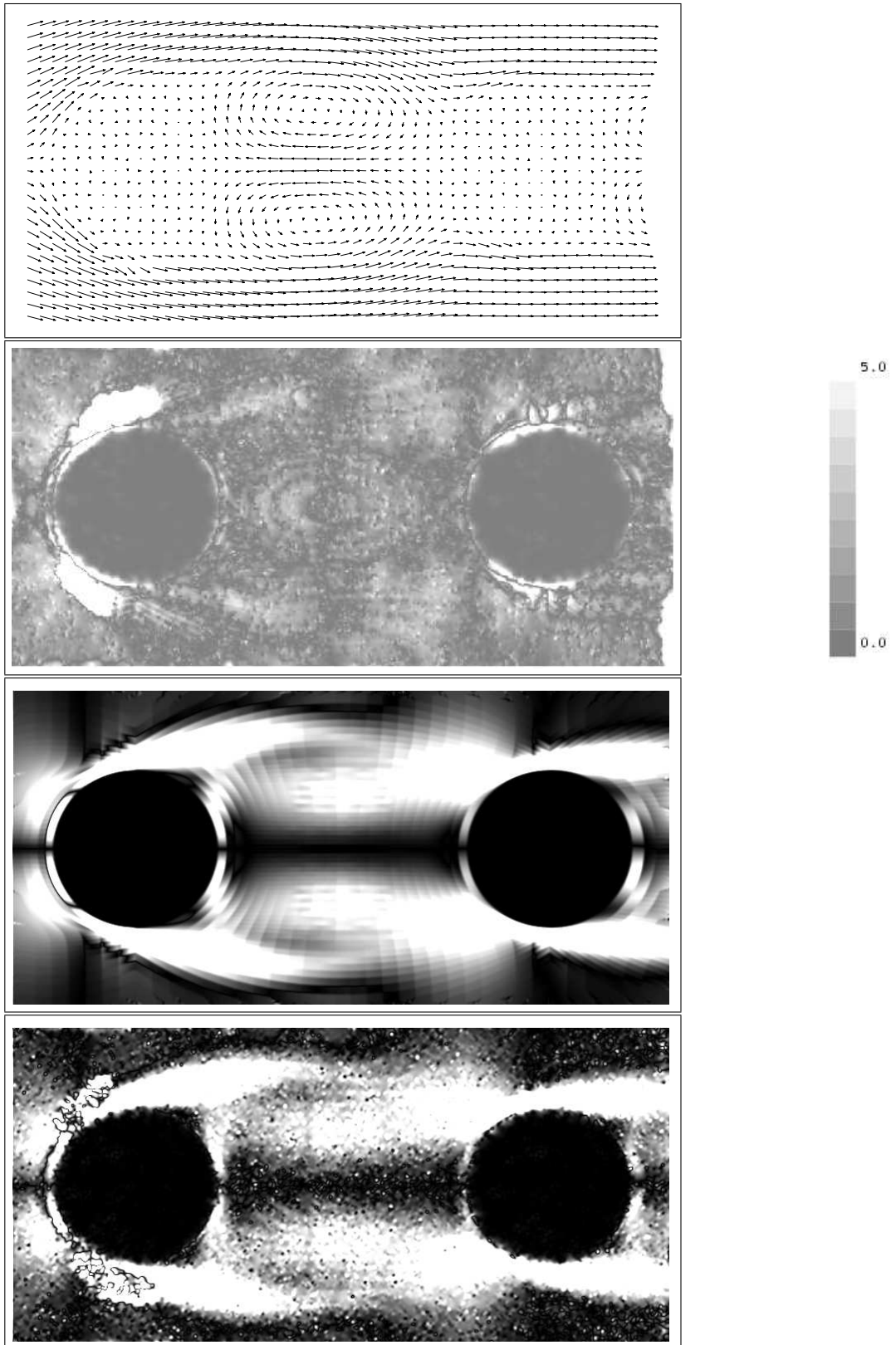


Figure 13: Results for the Quénot image pair “Mixed 20%”. Estimated flow field with H&S R+S (top), absolute displacement error (2nd row), exact vorticity field (3rd row) and estimated vorticity field (bottom).

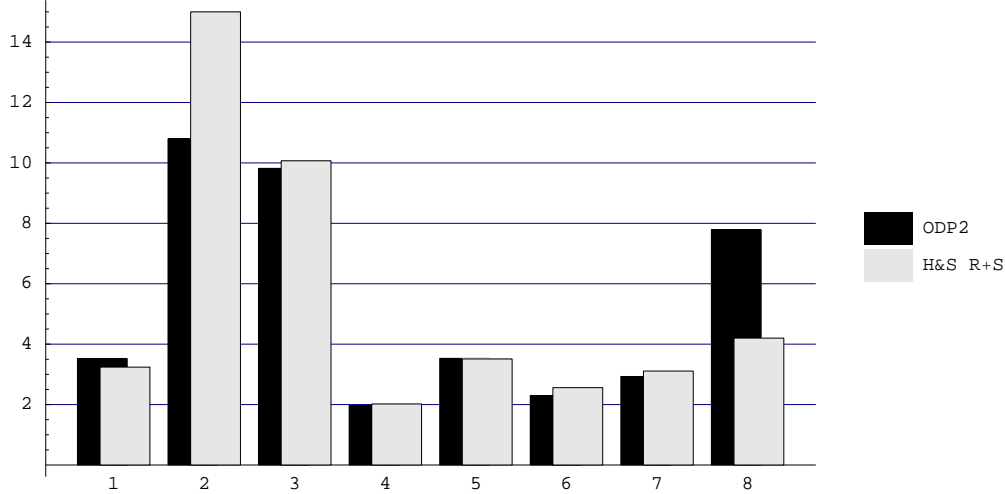


Figure 14: Average relative L_1 error of ODP2 and H&S R+S for the VSJ standard images pairs 01-08.

parameter of the image that influences the quality of the flow field estimation most.

In the VSJ standard image pairs 01 and 03-07, the error measures of ODP2 and H&S R+S are more or less equal. This coincides with the results of the “perfect” Quénot image pair since both image pairs have comparable average displacements, and the out-of-plane velocity is very low in these VSJ image pairs.

The error measures for image pair 02 and image pair 08 are most interesting since they clearly exhibit the different strengths of both approaches:

- Both approaches yield high error measures for image pair 02. This is no surprise since the average velocity is quite high in this example so that temporal aliasing becomes a severe problem. Though we used a coarse-to-fine strategy and multi-scale computations, the Taylor series linearization leads to errors that are higher than those of the ODP2 approach.
- Image pair 08, on the other hand, confirmed the results obtained for the Quénot image pair: While H&S R+S is tolerant towards noise (here mainly caused by out-of-plane velocity), ODP2 tends to much higher error measures when noise is present in the images.

Figure 15 shows that our approach is rather insensitive to changes of the smoothness parameter λ . However, if we adapted this parameter manually for every image pair, we could even achieve better error measures than the ones shown in figure 14.

4.4.3 Results on Real-World Image Pairs

Figures 16 and 17 show the results for the first real-world image pair (“cylinder wake”) computed with the variational approach and DPIV, respectively. One can clearly see that the variational approach resembles the true motion field much better than the cross-correlation approach. At regions with abruptly changing motion (i.e. the turbulence emerging behind the cylinder in the middle of the image), the DPIV method is not able to accurately determine the velocity field. This is mainly due to the limited spatial resolution, which leads to a violation of the assumption of a constant velocity inside interrogation windows at these locations. The statistical character of correlation-based processing, however, prohibits the use of smaller interrogation

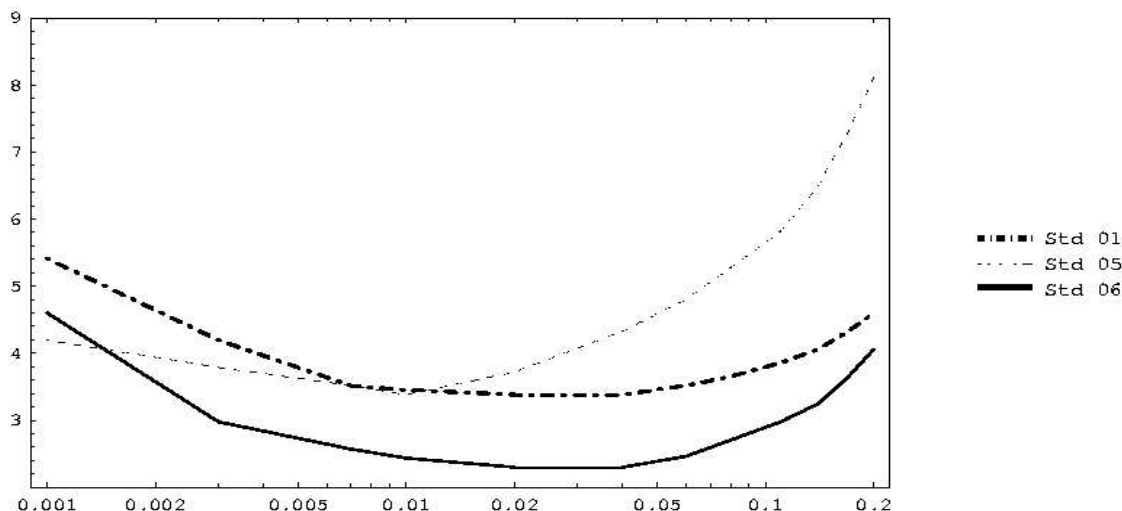


Figure 15: Average relative L_1 error of H&S R+S for the VSJ standard images pairs 01, 05, and 06 for changing smoothness parameters λ .

windows. Furthermore, in regions dominated by out-of-plane velocities (i.e. at the left border of the image), the cross correlation approach fails as well: Since no global velocity information is used, the probability of outliers is markedly increased at these locations, hence a valid flow field cannot be computed.

Figure 18 compares the H&S R+S results of the “freezing” image sequence with the results that Quénot achieved with ODP2. Both results resemble the true motion field very well. With the exception of the borders (where the gray value is constant and therefore no reliable motion can be estimated) and one spot in the middle of the image (where the velocity is high and varies locally very strongly), the absolute L_1 difference is persistently smaller than 0.5 pixels. From the visual impression, however, it is impossible to tell which of the two estimates is more precise.

5 Conclusions and Further Work

We have successfully applied a prototypical variational optical flow estimation approach to Particle Image Velocimetry. The novel approach outperforms the standard cross correlation methods and computes dense motion fields. We also compared our approach to ODP2, a sophisticated optical flow technique that is often used for PIV code validation. While ODP2 led to slightly better results for noise-free image pairs, our approach produces better results for noise levels of 5% and above. As a result, we expect that our variational optical flow estimation approach will perform better in real-world routine computations.

A decisive advantage of the variational approach (7) is its potential for further developments. Note that the data term (first term in (7)) was originally designed for images from everyday scenes (e.g. traffic scenes) whose gray value functions f are quite different and more well-behaved than PIV-sequences, from the signal processing point-of-view. While we tried to cope with this difficulty by carefully designing a coarse-to-fine representation of the image data (section 3), alternative data terms are conceivable, in particular in the critical case of low particle densities. Furthermore, the data term could be expanded to additionally estimate parameters of an illumination model to cope with the fact that local intensity changes are common in PIV image sequences. Similarly, various extensions of the simple smoothness term in (7) are possible,

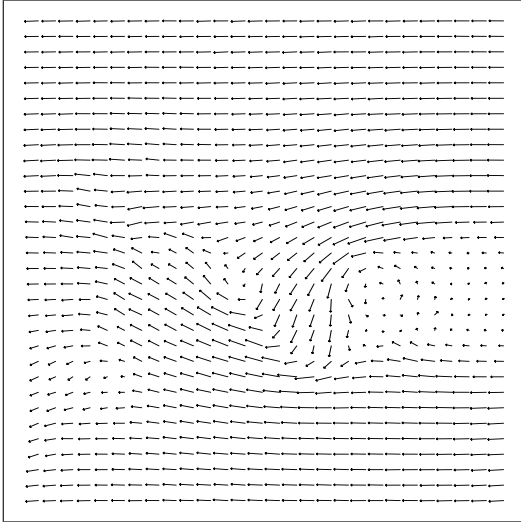


Figure 16: Dense vector field computed with the variational approach

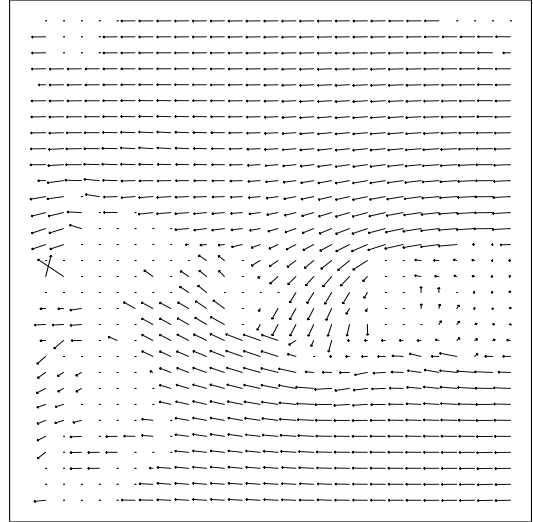


Figure 17: None-dense vector field computed with DPIV

such as spatio-temporal regularization [24], div-curl-shear regularization [20] or non-quadratic discontinuity-preserving regularization [23], for instance. Furthermore, one could add the possibility of specifying border conditions for regions where a liquid rinses a solid. Finally, the mathematical formulation leads to sound parallel implementations using off-the-shelf hardware [4, 10, 11].

References

- [1] BARRON, J., FLEET, D., AND BEAUCHEMIN, S., Performance of optical flow techniques. *IJCV*, 39:43–77,1994.
- [2] BRANDT, A., Multi-level adaptive solutions to boundary-value problems. *Mathematics of Computation*, 31(138):333-390, 1977.
- [3] BREDE, M., LEDER, A., AND WESTERGAARD, C.H., Time-resolved PIV investigation of the separated shear layer in the transitional cylinder wake. In *Proc. 5th Int. Symp. on PIV, (PIV'03), Busan, Korea, 2003*.
- [4] BRUHN, A., WEICKERT, J., FEDDERN, C., KOHLBERGER, T., AND SCHNÖRR, C., Variational optic flow computation in real-time. *IEEE Trans. Image Proc.*, in press.
- [5] CHETVERIKOV, D., Applying Feature Tracking to PIV *IJPRAI*, 17 (4):477–504, 2003.
- [6] CIARLET, P.G., *The Finite Element Method for Elliptic Probl.*. North-Holland Publ. Comp., Amsterdam, 1978.
- [7] HACKBUSCH, W., *Multigrid Methods and Applications*. Springer, New York, 1985.
- [8] HACKBUSCH, W., *Iterative Solution of Large Sparse Systems of Equations*. Springer-Verlag, 1993.
- [9] HORN, B.K.P., AND SCHUNCK, B.G., Determining optical flow. *Artif. Intell.*, 17: 185–203, 1981.
- [10] KOHLBERGER, T., SCHNÖRR, C., BRUHN, A., AND WEICKERT, J., Domain decomposition for variational optical flow computation. *IEEE Trans. Image Proc.*, in press.
- [11] KOHLBERGER, T., SCHNÖRR, C., BRUHN, A., AND WEICKERT, J., Parallel Variational Motion Estimation by Domain Decomposition and Cluster Computing. In T. Pajdla and J. Matas, editors, *Proc. ECCV 2004*, volume 3024, 205–216. Springer, 2004.

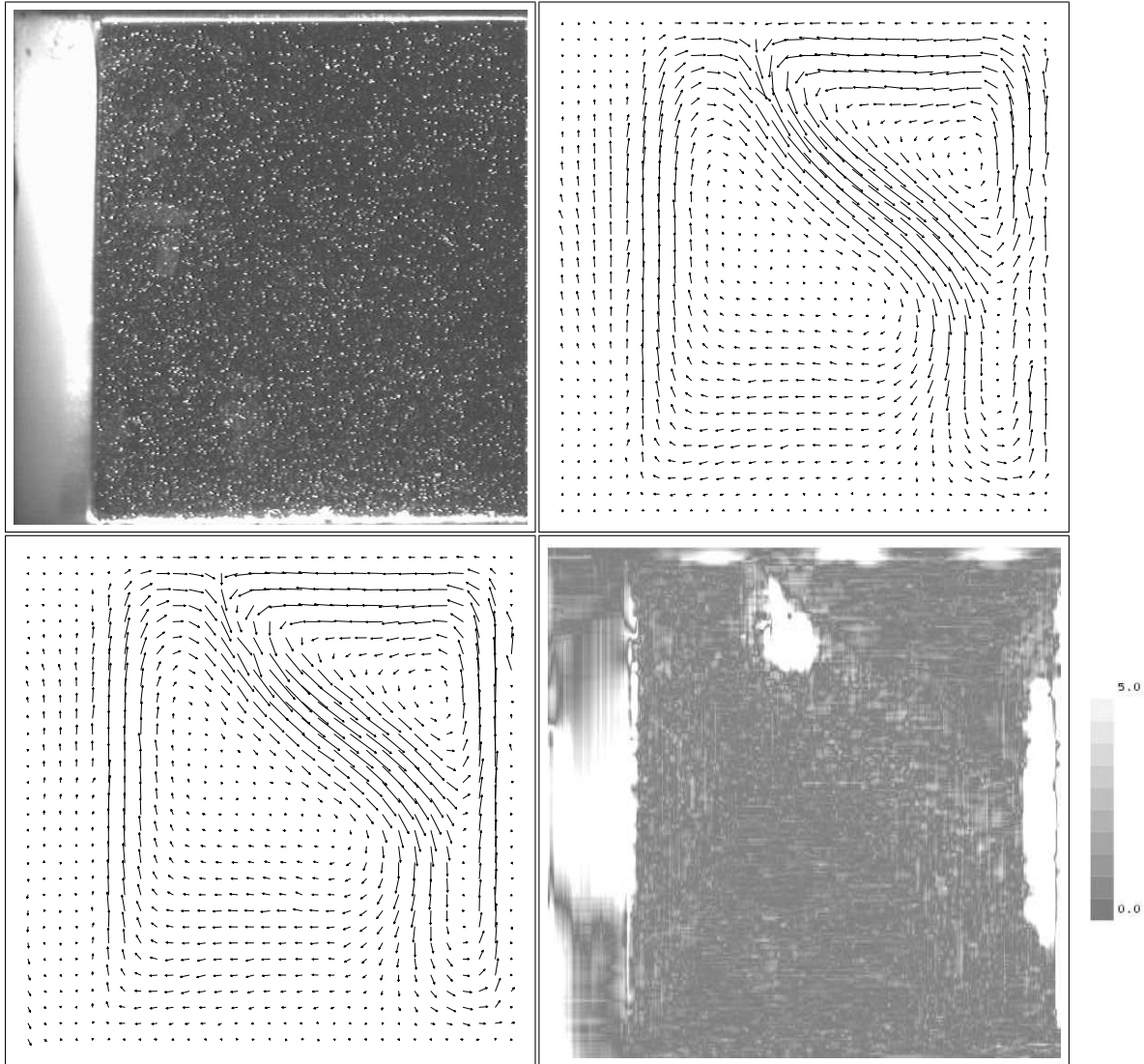


Figure 18: Freezing in a differentially heated cavity. Top row: Particle image and computed velocity field (H&S R+S). Bottom row: Velocity field computed with ODP2 (left), comparison of the absolute displacement values of the two solutions (right).

- [12] KRISHNAMURTHY, R., MOULIN, P., AND WOODS, J. Multiscale motion models for scalable video coding, 1996.
- [13] OKAMOTO, K., NISHIO, S., SAGA, T., AND KOBAYASHI, T., Standard images for PIV. *MST 11* 685–691, 2000.
- [14] QUÉNOT, G. M., Performance Evaluation of an Optical Flow Technique applied to PIV using the VSJ Standard Images. *Third International Workshop on PIV* 579–584, 1999.
- [15] QUÉNOT, G. M., The orthogonal algorithm for optical flow detection using dynamic programming *Intl. Conf. on Acoustics, Speech and Signal Proc.* 249–252, 1992.
- [16] QUÉNOT, G. M., PAKLEZA, J., AND KOWALEWSKI, T. A., PIV with optical flow. *Exp.Fluids*, 25: 177–189, 1998.
- [17] RAFFEL, M., WILLERT, C., AND KOMPENHANS, J., *Particle Image Velocimetry*. Springer, 2nd edition, 2001.
- [18] SCARANO, F., Iterative image deformation methods in PIV. *MST*, 13: R1–R19, 2002.
- [19] SCHNÖRR, C., Determining optical flow for irregular domains by minimizing quadratic functionals of a certain class. *Int. J. of Comp. Vision*, 6(1): 25–38, 1991.

- [20] SCHNÖRR, C., Segmentation of visual motion by minimizing convex non-quadratic functionals. In *12th Int. Conf. on Pattern Recognition*, Jerusalem, Israel, Oct 9-13 1994.
- [21] SCHNÖRR, C., Variational methods for adaptive image smoothing and segmentation. In B. Jähne, H. Haußecker, and P. Geißler, editors, *Handbook on Computer Vision and Applications: Signal Processing and Pattern Recognition*, volume 2, 451–484, San Diego, 1999. Academic Press.
- [22] SIMONCELLI, E. P., *Distributed Representation and Analysis of Visual Motion*. PhD thesis, MIT, 1993.
- [23] WEICKERT, J. AND SCHNÖRR, C., A theoretical framework for convex regularizers in pde-based computation of image motion. *IJCV*, 45(3): 245–264, 2001.
- [24] WEICKERT, J., AND SCHNÖRR, C., Variational optic flow computation with a spatio-temporal smoothness constraint. *J. Math. Imaging and Vision*, 14(3): 245–255, 2001.
- [25] WESTERGAARD, C.H., BREDE, M., AND LEDER, A., Time-space analysis of time resolved PIV data. In *Proc. 5th Int. Symp. on PIV (PIV'03)*, Busan, Korea, 2003.